APPLICATION OF UNSTEADY AERODYNAMIC METHODS FOR TRANSONIC AEROELASTIC ANALYSIS

ICAS-88-5.5.3

Woodrow Whitlow, Jr.*
NASA Langley Research Center
Hampton, Virginia 23665-5225 USA

Abstract

Aerodynamic methods for aeroelastic analysis are applied to various flow problems. These methods include those that solve the three-dimensional transonic small disturbance (TSD) potential equation, the two-dimensional (2-D) full potential (FP) equation, and the 2-D thin-layer Navier-Stokes equations. Flutter analysis performed using TSD aerodynamics shows that such methods can be used to analyze some aeroelastic phenomena. For thicker bodies and larger amplitude motions a nonisentropic full potential method is presented. The unsteady FP equation is modified to model the entropy jumps across shock waves. The conservative form of the modified equation is solved in generalized coordinates using an implicit, approximate factorization method. Pressures calculated on the NLR 7301 and NACA 64A010A airfoils using the nonisentropic FP method are presented. It is shown that modeling shock-generated entropy extends the range of validity of the FP method. A Navier-Stokes code is correlated with pressures measured on a supercritical airfoil at transonic speeds. When corrections are made for wind tunnel wall effects, the calculations correlate well with the measured data.

Introduction

Modern aircraft typically operate at high speeds where aeroelastic instabilities are more likely to occur. To successfully predict and analyze such phenomena, aeroelasticians need methods that predict accurately the aerodynamic loads that the vehicle experiences. Since many critical aeroelastic phenomena occur at transonic speeds, methods based on linear aerodynamic theory cannot accurately model these aeroelastic responses. Thus, it is necessary to use aerodynamic methods that can predict accurately time-dependent nonlinear flows.

The mathematical formulation that is used to model the flow is determined by the aeroelastic response that is to be analyzed. Flows may be modeled using a velocity potential equation, the Euler equations, or a form of the Navier-Stokes equations. Because of the extensive computer resources required to solve the Euler or Navier-Stokes equations[1], the primary tools used to calculate nonlinear aerodynamic phenomena are transonic small disturbance (TSD) codes[2,3] that can be interacted with viscous boundary layer methods. Many key aeroelastic phenomena, such as the minimum in flutter boundaries usually observed at transonic speeds (the transonic "flutter dip") can be analyzed using potential/boundary layer aerodynamics.[1]

To provide accurate predictions of transonic aeroelastic phenomena, aerodynamic methods should model accurately embedded shock waves and their unsteady motions. When shock waves form in transonic flow fields, aerodynamic loads predicted using isentropic potential methods can be highly inaccurate and even multivalued.[4-8] Thus, aeroelastic analysis performed using these loads does not always yield correct results. One reason for the inaccuracy is that isentropic potential theory models neither the entropy nor the vorticity produced when shock waves are present in transonic flow fields.

Fuglsang and Williams[9] modeled the effects of shock-generated entropy in two-dimensional (2-D) TSD theory, and Gibbons et al.[7] extended their method to three dimensions. Including these effects in the calculations resulted in TSD methods that model the Euler equations more accurately and that do not yield multiple solutions. Batina[10] added to the methods of refs. 7 and 9 by including corrections for vorticity as well as entropy in TSD theory. Whitlow et al.[8] developed a nonisentropic unsteady full potential method that is an extension of the steady flow method of Hafez and Lovell.[11] Nonisentropic effects of embedded shock waves are modeled by modifying the isentropic density to include the effects of shock-generated entropy.

Having developed methods for calculating inviscid flows, it is necessary to assess the accuracy of unsteady viscous boundary layer methods and to provide data to help guide the development of new techniques. One way in which this may be accomplished is comparisons of interacted inviscid/viscous calculations with results from Navier-Stokes codes. Rumsey and Anderson[12] have developed a Navier-Stokes code (CFL2D) for computing unsteady flows past airfoils. This code can be used to assess interacted unsteady inviscid/viscous methods and to help aid in the development of new unsteady boundary layer methods.

In the present effort, the nonisentropic full potential (NFP) method of Whitlow et al.[8] is implemented in a computer code and applied to AGARD standard airfoils for validation. The method allows accurate prediction of inviscid unsteady aerodynamic loads at relatively low computational expense. Comparisons of NFP pressures with Euler pressures and with pressures measured on AGARD standard airfoils are presented. These comparisons show that the range of validity of potential flow theory is extended when the nonisentropic effects of shock waves are modeled. The CFL2D code is correlated with steady pressures measured on a 14 percent thick supercritical airfoil. Pressures were measured at Reynolds numbers ranging from 5 million to 35 million.[13] In this paper, comparisons of calculated and measured pressures at Reynolds numbers of 6 million and 30 million are presented. The correlation with steady pressures is the initial step in an effort to correlate CFL2D with unsteady pressure data. The results of this longer range effort will provide a means of assessing interacted unsteady inviscid/viscous flow methods and will provide data to help guide the development of new unsteady boundary layer techniques. Meeting the long range goal will advance the capabilities of aeroelastic analysis methods.

Transonic Small Disturbance Methods

For attached flows on thin bodies at small angles of attack, methods based on transonic small disturbance (TSD) theory can be used for many aeroelastic applications. One code that can be used is CAP-TSD (Computational

*Group Leader, Unsteady Aerodynamics Branch, Loads and Aeroelasticity Division, Member AIAA.

Aeroelasticity Program-Transonic Small Disturbance).[3] It uses finite differences to solve the TSD potential equation

$$M^2(\phi_t+2\phi_x)_t = [(1-M^2)\phi_x+F\phi_x^2+G\phi_y^2]_x + (\phi_y+H\phi_x\phi_y)_y+(\phi_z)_z \quad (1)$$

where ϕ is the disturbance velocity potential, M is the free stream Mach number, t is time, and x,y,z are the spatial coordinate directions. For transonic flows, the coefficients F,G, and H are defined as

$$F = -\frac{1}{2}(\gamma+1)\,M^2$$

$$G = \frac{1}{2}(\gamma-3)\,M^2 \quad (2)$$

$$H = -(\gamma-1)\,M^2$$

where γ is the ratio of specific heats. In addition to solving the nonlinear equation (1), solutions of the linear potential equation may be obtained by setting F,G, and H to zero. Time-accurate solutions of (1) are obtained using an efficient approximate factorization algorithm.

The CAP-TSD code was used to compute the flutter boundary of a 45 degree swept wing[14]. Comparisons of the linear and nonlinear CAP-TSD flutter boundaries with experimental data are shown in fig. 1, taken from ref. 14. Shown in the figure are the flutter speed index (fig. 1(a)) and flutter frequency ratio (fig. 1(b)) versus Mach number. The experimental flutter data define a typical transonic flutter dip with the bottom near M = 1.0. Differences between the linear and nonlinear TSD flutter boundaries are due to nonlinear effects of transonic flow. The nonlinear CAP-TSD flutter boundary is slightly conservative in comparison with the experimental speed index. Generally, comparison of the nonlinear flutter boundaries with experimental data is good, which provides an initial step toward validating TSD methods for transonic aeroelastic applications.

Although methods based on TSD theory can be used to analyze significant aeroelastic problems, when bodies are thick or the amplitude of motion is large, TSD methods may be unreliable. Thus, full potential methods are being developed.

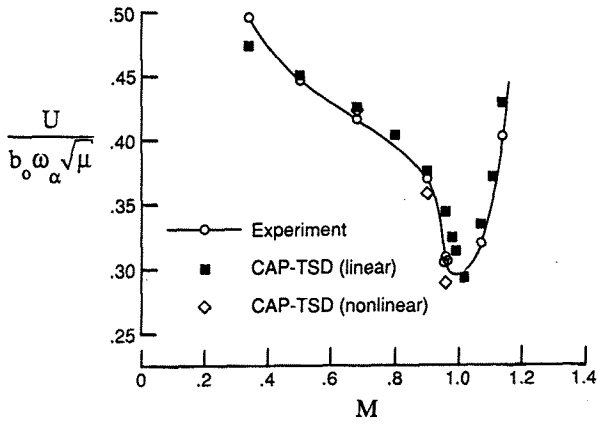

(a) flutter speed index versus Mach number

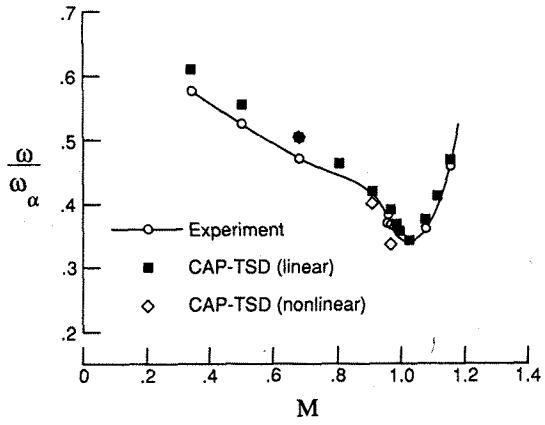

(b) flutter frequency ratio versus Mach number

Fig. 1. Comparisons of CAP-TSD and measured flutter boundaries for 45° swept wing in air.

Full Potential Methods

When calculating transonic flows past thick bodies or bodies undergoing large amplitude motions, it is typical for strong shock waves to form in the flow field. This can cause aerodynamic loads predicted using potential methods to be highly inaccurate and even multivalued. Multiple solutions of the potential equation were first observed in 2-D flow by Steinhoff and Jameson.[4] Salas and Gumbert[5] showed that the phenomenon is not confined to a particular airfoil or flow condition. Williams et al.[6] calculated multiple solutions using 2-D TSD theory, and Gibbons et al.[7] showed multiple TSD solutions for high-aspect-ratio wings. For lower-aspect-ratio wings, multiple solutions were not observed, but calculated loads were highly inaccurate when shock waves formed in the flow field.

One reason for the inaccuracy of isentropic potential theory is that it does not model the entropy change that a fluid particle experiences as it passes through shock waves. In this section, that shortcoming is addressed by the presentation of a nonisentropic unsteady full potential (FP) method. The present method is an extension of the steady FP method of Hafez and Lovell.[11]

In cartesian coordinates, the flow field is described by the 2-D unsteady FP equation in conservation form

$$\rho_t + (\rho\Phi_x)_x + (\rho\Phi_z)_z = 0 \quad (3)$$

where Φ is the velocity potential, and ρ is the isentropic density. In generalized coordinates, given by the transformation

$$\xi = \xi\,(x,z,t)$$

$$\zeta = \zeta\,(x,z,t) \quad (4)$$

$$\tau = t$$

strong conservation form of (3) is maintained by writing the continuity equation in transformed coordinates as

$$\left(\frac{\rho}{J}\right)_\tau + \left(\frac{\rho U}{J}\right)_\xi + \left(\frac{\rho W}{J}\right)_\zeta = 0 \tag{5}$$

In (4) and (5), ξ and ζ are the computational coordinate directions around and normal to the airfoil, τ is computational time, and U and W are the contravariant velocities in the ξ and ζ directions, respectively, given by

$$\begin{aligned} U &= \xi_t + A_1\Phi_\xi + A_2\Phi_\zeta \\ W &= \zeta_t + A_2\Phi_\xi + A_3\Phi_\zeta \end{aligned} \tag{6}$$

The metric terms, A_1, A_2, and A_3, are related to the computational coordinate directions by

$$\begin{aligned} A_1 &= \xi_x^2 + \xi_z^2 \\ A_2 &= \xi_x\zeta_x + \xi_z\zeta_z \\ A_3 &= \zeta_x^2 + \zeta_z^2 \end{aligned} \tag{7}$$

and the Jacobian of the transformation J is

$$J = \xi_x\zeta_z - \xi_z\zeta_x \tag{8}$$

Entropy-Correction Method

When a fluid particle passes through a shock wave it experiences a change in entropy Δs which is a function of the upstream Mach number normal to the shock M_n

$$\frac{\Delta s}{R} = \frac{1}{\gamma - 1}\left\{\ln\left(\frac{2\gamma}{\gamma+1}M_n^2 - \frac{\gamma-1}{\gamma+1}\right) - \gamma\ln\left[\frac{(\gamma+1)M_n^2}{(\gamma-1)M_n^2+2}\right]\right\} \tag{9}$$

where R is the gas constant. For unsteady flows, the shock speed must be monitored to obtain the correct value of M_n. The nonisentropic density is

$$\rho = \rho_i e^{\frac{-\Delta s}{R}} \tag{10}$$

where ρ_i is the isentropic density from equation (3). Substituting (10) into the continuity equation, (5), yields

$$\left(\frac{\rho_i e^{\frac{-\Delta s}{R}}}{J}\right)_\tau + \left(\frac{\rho_i e^{\frac{-\Delta s}{R}} U}{J}\right)_\xi + \left(\frac{\rho_i e^{\frac{-\Delta s}{R}} W}{J}\right)_\zeta = 0 \tag{11}$$

Equation (11) is solved using first order backward differencing in time and second order central differencing in space. The time derivative of density is linearized about previous time levels such that conservation form is maintained. The resulting equation is factored into

$$\begin{aligned} L_\xi L_\zeta \Delta\Phi &= (\Phi^n - \Phi^{n-1}) + \frac{\beta^{n-1}}{\beta^n}(\Phi^n - 2\Phi^{n-1} + \Phi^{n-2}) \\ &+ \frac{h}{\beta^n}(\bar\rho^n - \bar\rho^{n-1}) \\ &+ h\frac{\beta^{n-1}}{\beta^n}(U^{n-1}\delta_\xi + W^{n-1}\delta_\zeta)(\Phi^n - \Phi^{n-1}) \\ &+ \frac{h^2}{\beta^n}\left[\delta_\xi\left(\frac{\bar\rho U}{J}\right)^n + \delta_\zeta(\bar\rho W)^n - F_\infty\right] \end{aligned} \tag{12}$$

where

$$L_\xi = \left[I + hU^n\delta_\xi - \frac{h^2}{\beta^n}\delta_\xi(\bar\rho A_1)^n\delta_\xi\right]$$

$$L_\zeta = \left[I + hW^n\delta_\zeta - \frac{h^2}{\beta^n}\delta_\zeta(\bar\rho A_3)^n\delta_\zeta\right]$$

$$\Delta\Phi = \Phi^{n+1} - \Phi^n$$

$$h = \Delta\tau$$

$$\bar\rho = \frac{\rho_i e^{\frac{-\Delta s}{R}}}{J}$$

$$\beta = \frac{\left(\rho_i e^{\frac{-\Delta s}{R}}\right)^{2-\gamma}}{J}$$

The terms $\delta\xi$ and $\delta\zeta$ represent central difference operators, superscripts n-1, n, and n+1 represent computational time levels, and F_∞ is a correction to the residual due to incomplete metric cancellation.[15,16]

To introduce artificial viscosity into the difference scheme and calculate shock waves, a flux-biased differencing method[17,18] is used to discretize the flow equations. The density $\tilde\rho$, biased in the ξ direction, is given by

$$\tilde\rho = \frac{1}{q}\left[\rho_i e^{\frac{-\Delta s}{R}} q - \Delta\xi(\rho q)_\xi^-\right] \tag{13}$$

where

$$(\rho q)^- = \begin{cases} \rho_i e^{\frac{-\Delta s}{R}} q - \rho^* q^* & q > q^* \\ 0 & q \le q^* \end{cases} \tag{14}$$

q is the flow speed, and q^* and ρ^* are the sonic speed and density, respectively. For steady flows, ρ^* and q^* are constants that are computed once per calculation. For unsteady flows, ρ^* and q^* must be computed throughout the flow field at each time step. Flux biasing (a) accurately tracks sonic conditions and automatically specifies the correct amount of artificial viscosity, (b) produces no velocity overshoots, allowing for larger time steps for unsteady calculations, (c) produces monotone shock profiles with a maximum two point transition between the upstream

and downstream states, and (d) dissipates expansion shock waves, ruling out solutions with such nonphysical characteristics.

For lifting flows, the shed vorticity is represented as a jump in potential across a wake line. The nonisentropic wake condition is determined by requiring that the pressure and normal velocity be continuous across the wake. The nonisentropic pressure coefficient Cp is given by

$$C_p = \frac{2}{\gamma M^2}\left[\rho_i e^{\left(\frac{-\Delta s}{R}\right)\gamma} - 1\right]$$

and the zero pressure jump condition is enforced by requiring that

$$\left(\rho_i e^{\frac{-\Delta s}{R}}\right)^u = \left(\rho_i e^{\frac{-\Delta s}{R}}\right)^l$$

This results in the following condition for the jump in potential

$$\Gamma_\tau + \langle W \rangle \Gamma_\zeta = \left[\left(e^{\frac{-\Delta s}{R}}\right)^u - \left(e^{\frac{-\Delta s}{R}}\right)^l\right]$$

$$- \frac{1}{\gamma - 1}\left[\left(\rho_i^{\gamma-1} - 1\right)^u \left(\frac{\Delta s}{R}\right)^u - \left(\rho_i^{\gamma-1} - 1\right)\left(\frac{\Delta s}{R}\right)^l\right]$$

where Γ is the jump in potential across the wake, $\Phi^u - \Phi^l$, and $\langle W \rangle$ is the average of W above and below the wake. For flows with no shock waves and hence no entropy production, the wake condition reduces to the isentropic condition.[19]

To assess the nonisentropic full potential method, pressures were calculated on the NLR 7301 and NACA 64A010A airfoils using isentropic and nonisentropic methods. Comparisons of steady full potential and Euler pressures[20] on the NLR 7301 at a transonic high lift condition are presented. Comparisons of calculated unsteady lifting pressures and experimental data are presented for the NACA 64A010A oscillating in pitch about its quarter chord.

NLR 7301

In this section, calculations made for the NLR 7301 airfoil are presented. Fig. 2 shows a comparison of isentropic potential calculations and Euler calculations for M = 0.7 and angle of attack (α) = 2°. The shock wave calculated using the isentropic potential method is too strong and too far aft on the airfoil chord. This result suggests that this case is outside the range of validity of isentropic potential flow theory. Fig. 3 shows a comparison of nonisentropic full potential pressures with Euler pressures. Modeling the nonisentropic effects brings the potential flow pressures into good agreement with the Euler results. The locations of the calculated shock waves differ by only 3-4 percent of chord and have nearly the same strengths. The TSD results of ref. 10 suggest that modeling vorticity, as well as entropy effects, could further improve the comparisons.

NACA 64A010A

In this section, calculations for the NACA 64A010A airfoil are presented. The airfoil is the model of the NACA 64A010 airfoil that was tested at the NASA Ames Research Center.[21] That model has a small amount of camber and surface waviness. The experimental data presented here are for M = 0.796 and Reynolds number (Re) of 12.5 x 10^6.

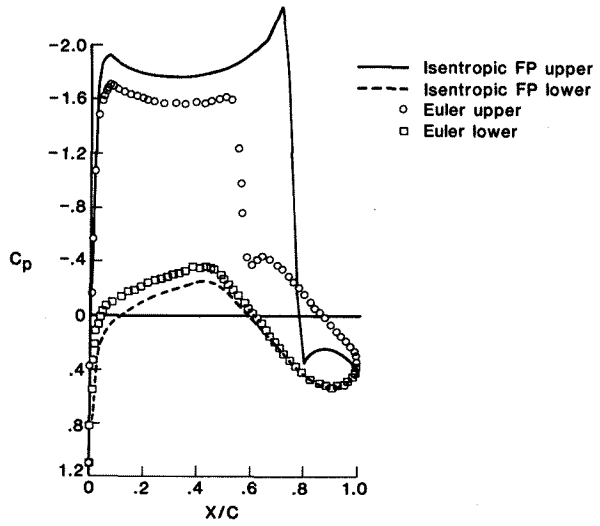

Fig. 2. Calculated isentropic potential and Euler steady pressures on NLR 7301 airfoil, M = 0.7, α = 2°.

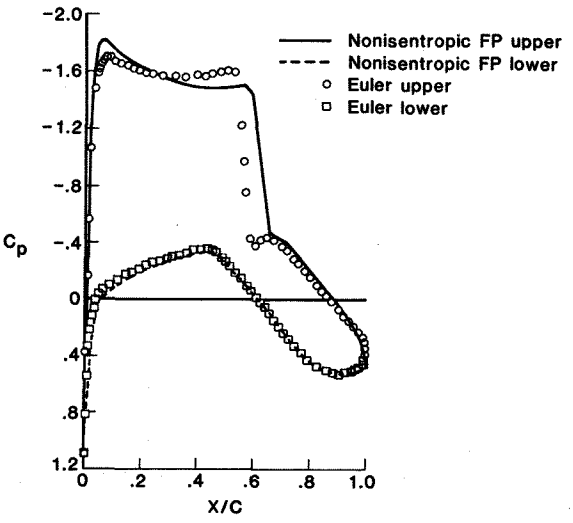

Fig. 3. Calculated nonisentropic potential and Euler steady pressures on NLR 7301 airfoil, M = 0.7, α = 2°.

Fig. 4 shows the measured and calculated steady pressures on the airfoil surface. The surface waviness is evident in the pressure distributions upstream of the midchord. Agreement between the calculations and experiment is good, with the level of calculated pressures upstream of midchord slightly above the measured values. On the forward portion of the airfoil, the isentropic and nonisentropic pressures are nearly the same, and no differences in the plotted pressures are evident. The calculated shock wave is 2-3 percent downstream of the measured location, is of moderate strength, and the effects of the nonisentropic corrections are to cause a slight weakening and forward shift of the shock. The differences between the measured and calculated pressures are as expected for comparison of inviscid methods with experimental data.

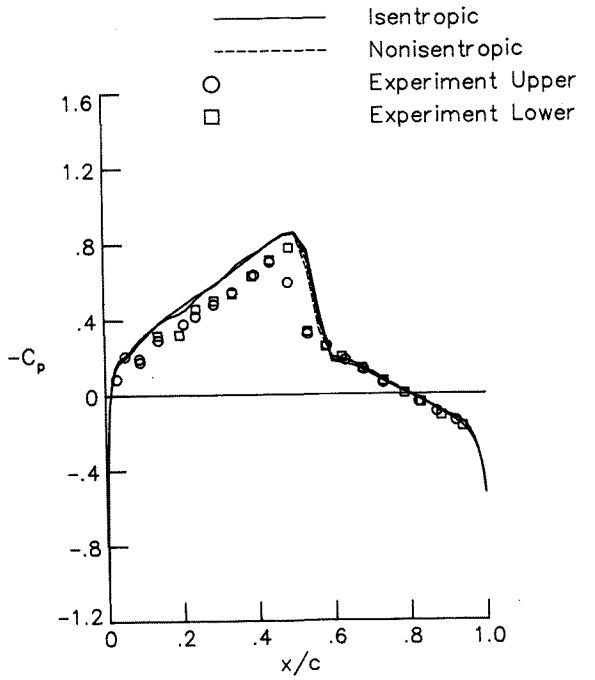

Fig. 4. Steady pressures on NACA 64A010A airfoil, M = 0.796, α = 0°.

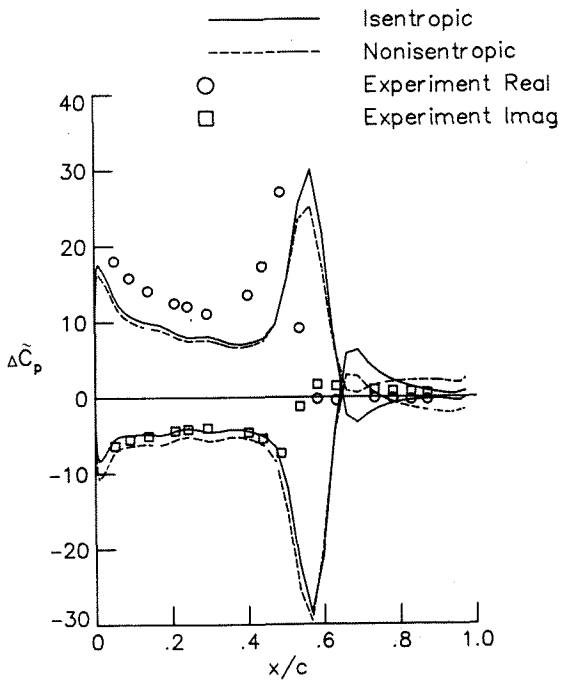

Fig. 5. First harmonic of unsteady lifting pressures on NACA 64A010A airfoil, M = 0.796, $\alpha = 1.02°\sin(k\tau)$, k = 0.051.

Unsteady pressures were calculated for the NACA 64A010A airfoil oscillating in pitch about its quarter chord, $\alpha(\tau) = \alpha_o \sin(k\tau)$. Fig. 5 shows the first harmonic of the unsteady lifting pressures for α_o = 1.02°, k = 0.051, where k is reduced frequency based on airfoil semichord. Except in the vicinity of the shock wave, the agreement between the calculations and experiment is generally good,with the better agreement shown with the out-of-phase component. The calculated shock pulse is downstream of and stronger than the measured pulse. For this case, the effect of the entropy corrections is to cause a slight shift forward and decrease in the amplitude of the shock pulse.

The first harmonic of the unsteady lifting pressure for α_o = 1.02°, k = 0.101 is shown in fig. 6. For this higher frequency case, the differences in the isentropic and nonisentropic potential calculations are more pronounced. The effects of the entropy corrections are to decrease the amplitude and width of the imaginary part of the shock pulse and to increase the amplitude of the real part. These effects result in improved agreement of the calculations with the measured data.

Fig. 7 shows the first harmonic of the unsteady lifting pressure for α_o = 2°, k = 0.101. Except for the shock pulse being downstream of the measured location, the agreement between the nonisentropic calculations and experiment is good. Modeling the nonisentropic effects causes an increase in the amplitude of the real part of the shock pulse and a decrease in the imaginary part. For both components of the lifting pressure, modeling shock -generated entropy results in improved agreement of the calculations with experiment.

Mohr et al.[22] used TSD with entropy and vorticity corrections to do flutter analysis of a generic transport wing. Flutter boundaries shown in figs. 10 and 11 of ref. 22 indicate the importance of modeling nonisentropic effects in potential flow methods.

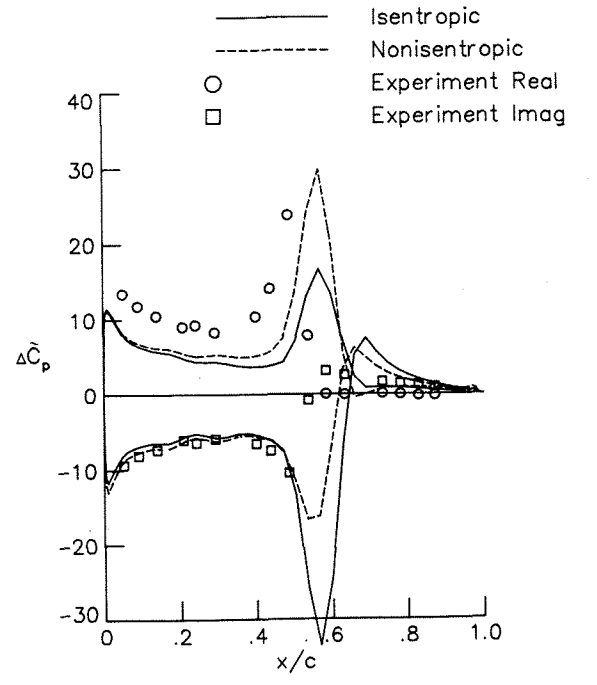

Fig. 6. First harmonic of unsteady lifting pressures on NACA 64A010A airfoil, M = 0.796, $\alpha = 1.02°\sin(k\tau)$, k = 0.101.

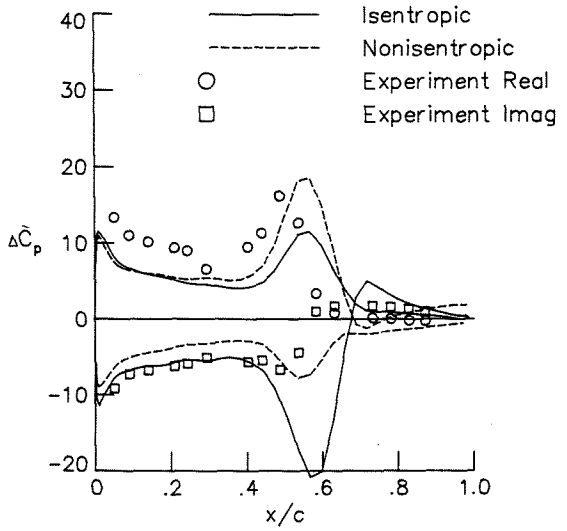

Fig. 7. First harmonic of unsteady lifting pressures on NACA 64A010A airfoil, M = 0.796, $\alpha = 2°\sin(k\tau)$, k = 0.101.

Navier-Stokes Methods

In the above sections, it is shown that potential flow methods can be used for analysis of aeroelastic phenomena when the flow is attached. Comparisons of computed and measured flutter boundaries usually show very good agreement at subsonic speeds, and as speed increases into the transonic regime, the boundaries tend to deviate. The minimum of the flutter boundary is a critical condition and represents a primary challenge for computational aeroelastic analysis. It is associated with the formation of shock waves and the onset of flow separation. Navier-Stokes methods could be used to analyze this phenomenon, but the required computer resources limits use of such methods.(1) This case may be treated using inviscid flow codes interacted with unsteady viscous boundary layer models.

There is a need to develop a data base for assessing the accuracy of unsteady interacting boundary layer methods and for providing data to help aid in the development of new methods. A Navier-Stokes code can be used for these purposes. For 2-D and strip boundary layer applications a 2-D code can be used. Here, pressures calculated using the CFL2D code(12) are correlated with measured transonic pressures. The calculations presented here are solutions of the thin-layer approximation to the Reynolds averaged equations. In the thin-layer approximation, viscous terms are resolved in a layer near the body, and only viscous terms normal to the body are retained. The algebraic eddy viscosity Baldwin-Lomax turbulence model(23) is used to calculate turbulent flow.

The pressures were measured on a fourteen percent thick supercritical airfoil in the 0.3 meter Transonic Cryogenic Tunnel at the NASA Langley Research Center.(13) The profile of the airfoil, designated Sc(2)-0714 is shown in fig. 8. Reynolds numbers for the test ranged from 5 million to 35 million, and comparisons to be presented here are for Reynolds numbers of 6 million and 30 million. For comparison with wind tunnel data, flow conditions corrected to account for wind tunnel wall interference are used as input into CFL2D. The angle-of-attack corrections depend on the lift, model chord, tunnel height, and the width and spacing of the slots.(24) Mach number corrections are functions of the model span and aspect ratio and sidewall boundary layer displacement thickness and shape factor.(25)

Fig. 8. Profile of Sc(2)-0714 supercritical airfoil.

Fig. 9 shows a comparison of calculated and measured pressures at Re = 6.01 million for corrected Mach number (M_c) and angle of attack (α_c) equal to 0.710 and 0.525°. The calculations are in good agreement with the measured data. On the upper surface, the level of CFL2D pressures upstream of the shock wave is only slightly lower than the measured values, and the calculated and measured shock strengths and locations are in good agreement. Downstream of the shock, correlation of calculated and measured pressures is very good. Fig. 10 shows a comparison of calculated and measured pressures at Re = 6.035 million, $M_c = 0.710$, $\alpha_c = 0.844°$. At this higher angle of attack, the agreement between the calculations and experiment remains good. The level of calculated pressures on the upper surface is only slightly less than the measured values, and the calculated shock wave is slightly upstream of the experimental location.

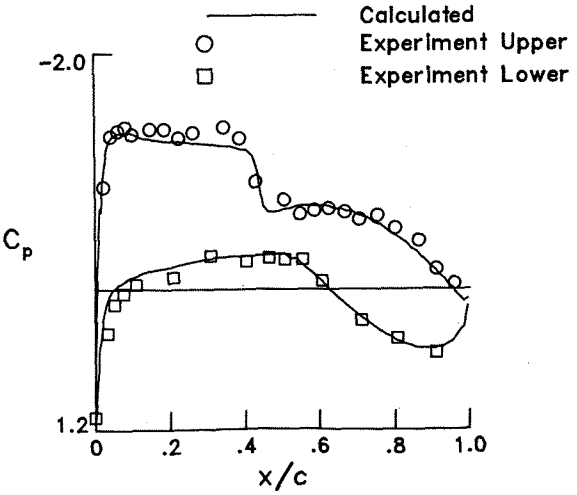

Fig. 9. Navier-Stokes and measured steady pressures on Sc(2)-0714 airfoil, $M_c = 0.710$, $\alpha_c = 0.525°$, Re = 6.01 x 10^6.

The next pair of comparisons is at the higher Reynolds number of 30 million. Fig. 11 shows a comparison of calculated and measured pressures for $M_c = 0.710$, $\alpha_c = 0.393°$, and comparisons for $M_c = 0.711$, $\alpha_c = 0.756°$ are shown in fig. 12. In both cases, the agreement between calculations and experiment is reasonably good, although there are slight differences in the locations of the computed and measured shock waves.

The results presented in figs. 9-12 show that CFL2D

predicts accurate steady pressures for a range of angles of attack and Reynolds numbers. This allow the code to be used to examine the effects of these parameters on computed flow fields. An illustration of angle-of-attack effects is shown in fig. 13. The calculations are for Re = 6 million, M = 0.710, α = 0.525° and 0.844°. These calculations show that increasing α causes increased expansion of the flow on the forward part of the airfoil upper surface and an increase in the level of pressures. The shock wave is strengthened and moved aft on the airfoil.

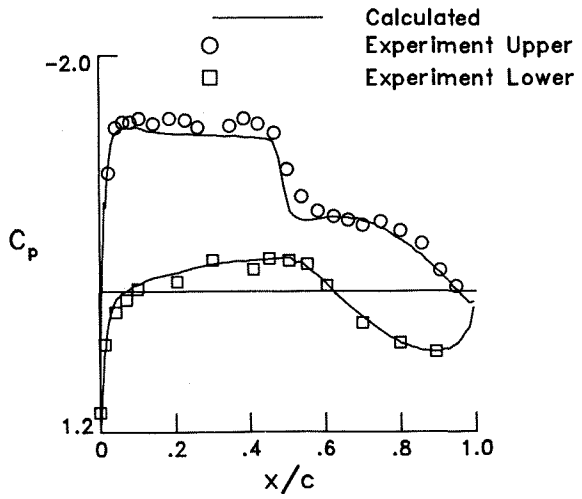

Fig. 10. Navier-Stokes and measured steady pressures on Sc(2)-0714 airfoil, M_c = 0.710, α_c = 0.844°, Re = 6.035 x 10^6.

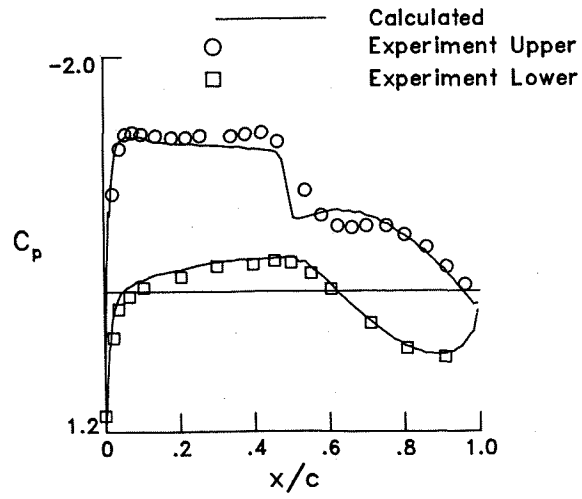

Fig. 11. Navier-Stokes and measured steady pressures on Sc(2)-0714 airfoil, M_c = 0.712, α_c = 0.393°, Re = 30 x 10^6.

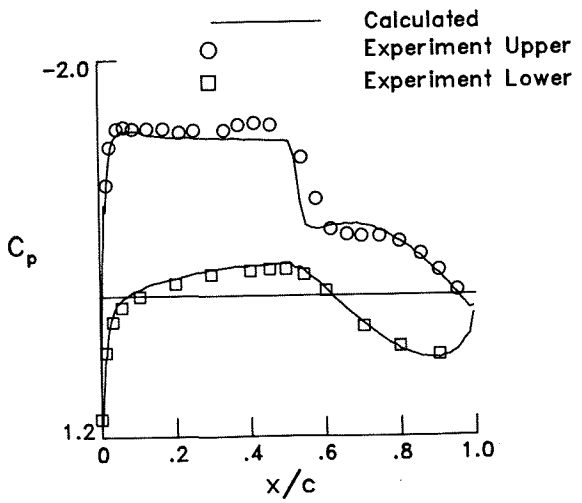

Fig. 12. Navier-Stokes and measured steady pressures on Sc(2)-0714 airfoil, M_c = 0.710, α_c = 0.756°, Re = 30 x 10^6.

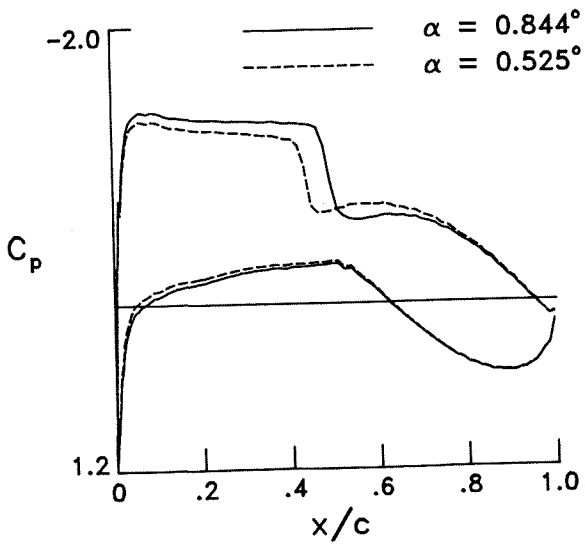

Fig. 13. Effect of angle of attack on Navier-Stokes steady pressures, Sc(2)-0714 airfoil, M = 0.710, Re = 6 x 10^6.

The effects of Reynolds number on the calculated pressures are shown in fig. 14. The calculations are for M = 0.710, α = 0.525°, Re = 6.01 million and 30 million. The primary effect of increasing the Reynolds number is to strengthen the shock wave and move it aft on the airfoil. This follows since increasing the Reynolds number decreases the influence of viscosity and causes the pressures to show more characteristics of those obtained in inviscid flows.

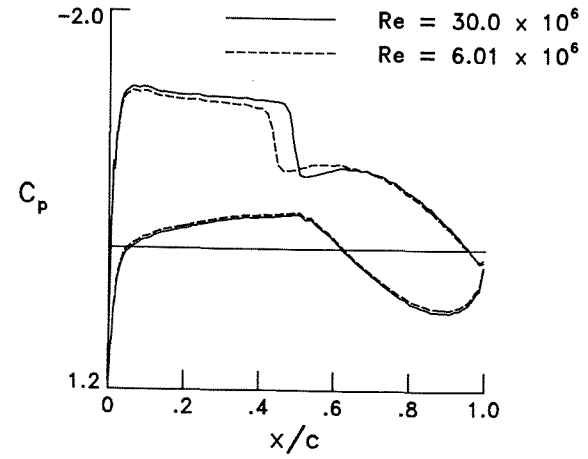

Fig. 14. Effect of Reynolds number on Navier-Stokes steady pressures, Sc(2)-0714 airfoil, M = 0.710, α = 0.525°.

Concluding Remarks

Methods for calculating aerodynamic loads have been presented and validated by comparing calculated and measured pressures on airfoils. Transonic small disturbance methods are applicable to thin bodies undergoing small-amplitude motions. For attached flows, these methods are shown to provide fairly accurate results for some aeroelastic analyses.

For thick bodies, full potential methods are being developed. To ensure accurate calculations at transonic speeds, the effects of shock-generated entropy are modeled. The resulting method was tested for the NLR 7301 and NACA 64A010A airfoils. Comparisons of calculated pressures with experimental data and with Euler calculations are presented for the NLR 7301 airfoil, and comparisons of calculated pressures with experimental data are presented for the NACA 64A010A airfoil. A strong shock case for the NLR 7301 airfoil shows that modeling nonisentropic effects can extend the range of validity of potential methods. Accurate solutions can be obtained at conditions for which isentropic potential methods fail. Calculations for the NACA 64A010A airfoil indicate that for shock waves of weak to moderate strength, modeling the nonisentropic effects has small effects on the steady pressures--slight weakening and forward shift of the shock wave. However, for some unsteady cases, the effects are significant.

Pressures calculated with the CFL2D code are correlated with those measured in the 0.3 meter transonic cryogenic tunnel at the NASA Langley Research Center. For correlation of the pressures, the wind tunnel flow conditions must be corrected to account for wall interference. When using the corrected flow conditions, the calculations show good agreement with the measured data.

References

[1]Whitlow, Woodrow, Jr.: Computational Unsteady Aerodynamics for Aeroelastic Analysis, NASA TM 100523, December 1987.

[2]Borland, C. J.; and Rizzetta, D. P.: Nonlinear Transonic Flutter Analysis, *AIAA Journal*, **Vol. 20**, No. 11, pp. 1606-1615, 1982.

[3]Batina, John T.; Seidel, David A.; Bland, Samuel R.; and Bennett, Robert M.: Unsteady Transonic Flow Calculations for Realistic Aircraft Configurations, AIAA 87-0850, 1987.

[4]Steinhoff, John; and Jameson, Antony: Multiple Solutions of the Transonic Potential Flow Equation, *AIAA Journal*, **Vol. 20**, No. 11, pp. 1521-1525, 1982.

[5]Salas, M. D.; and Gumbert, C. R.: Breakdown of the Conservative Potential Equation, AIAA 85-0367, 1985.

[6]Williams, Marc H.; Bland, Samuel R.; and Edwards, John W.: Flow Instabilities in Transonic Small Disturbance Theory, *AIAA Journal*, **Vol. 23**, No. 10, pp. 1491-1496, 1985.

[7]Gibbons, M. D.; Whitlow, W., Jr.; and Williams, M. H.: Nonisentropic Unsteady Three Dimensional Small Disturbance Potential Theory, AIAA 86-0863, 1986.

[8]Whitlow, W., Jr.; Hafez, M. M.; and Osher, S. J.: An Entropy Correction Method for Unsteady Full Potential Flows with Strong Shocks, *Journal of Fluids and Structures*, **Vol. 1**, pp. 401-414, 1987.

[9]Fuglsang, D. F.; and Williams, M. H.: Non-Isentropic Unsteady Transonic Small Disturbance Theory, AIAA 85-0600, 1985.

[10]Batina John T.: Unsteady Transonic Small Disturbance Theory Including Entropy and Vorticity Effects, AIAA 88-2278, 1988.

[11]Hafez, M.; and Lovell, D.: Entropy and Vorticity Corrections for Transonic Flows, AIAA 83-1926, 1983.

[12]Rumsey, Christopher L.; and Anderson, W. Kyle: Some Numerical and Physical Aspects of Unsteady Navier-Stokes Computations over Airfoils using Dynamic Meshes, AIAA 88-0329, 1988.

[13]Hess, Robert W.; Seidel, David A.; Igoe, William B.; and Lawing, Pierce L.: Highlights of Unsteady Pressure Tests on a 14 Percent Supercritical Airfoil at High Reynolds Number Transonic Condition, NASA TM 89080, January 1987.

[14]Bennett, Robert M.; Batina, John T.; and Cunningham, Herbert J.: Wing Flutter Calculations with the CAP-TSD Unsteady Transonic Small Disturbance Program, AIAA 88-2347, 1988.

[15]Bridgeman, J. O.; Steger, J. L.; and Caradonna, F. X.: A Conservative Finite Difference Algorithm for the Unsteady Transonic Potential Equation in Generalized Coordinates, AIAA 82-1388, 1982.

[16]Steger, Joseph L.: Implicit Finite Difference Simulation of Flow about Arbitrary Two-Dimensional Geometries, *AIAA Journal*, **Vol. 16**, No. 7, pp. 679-686, 1978.

[17]Hafez, M.; Osher, S.; and Whitlow, W., Jr.: Improved Finite Difference Schemes for Transonic Potential Calculations, *AIAA Journal*, **Vol. 25**, No. 11, pp. 1456-1462, 1987.

[18]Osher, S.; Hafez, M.; and Whitlow, W., Jr.: Entropy Condition Satisfying Approximation for the Full Potential Equation of Transonic Flow, *Mathematics of Computations*, **Vol. 44**, pp. 1-29, 1985.

[19]Whitlow, Woodrow, Jr.: Application of a Nonisentropic Full Potential Method to AGARD Standard Airfoils, AIAA 88-0710, 1988.

[20]Jameson, A.: Solution of the Euler Equations for Two Dimensional Transonic Flow by a Multigrid Method, Princeton University MAE Report No. 1613, 1983.

[21]Davis, Sandford S.; and Malcolm, Gerald N.: Experimental Unsteady Aerodynamics of Conventional and Supercritical Airfoils, NASA TM 81221, 1980.

[22]Mohr, Ross W.; Batina, John T.; and Yang, Henry T. Y.: Mach Number Effects on Transonic Aeroelastic Forces and Flutter Characteristics, NASA TM 100547, February 1988.

[23]Baldwin, B; and Lomax, H.: Thin Layer Approximations and Algebraic Model for Separated Turbulent Flows, AIAA 78-257, 1978.

[24]Barnwell, Richard W.: Design and Performance Evaluation of Slotted Walls for Two-Dimensional Wind Tunnels, NASA TM 78648, February 1978.

[25]Green, Lawrence L.; and Newman, Perry A.: Transonic Wall Interference Assessment and Corrections for Airfoil Data from the 0.3-Meter TCT Adaptive Wall Test Section, AIAA 87-1431, 1987.